ELSEVIER

Ceramics International 33 (2007) 1007–1018

CERAMICS INTERNATIONAL

www.elsevier.com/locate/ceramint

Degradation mechanisms of magnesia-carbon refractories by high-alumina stainless steel slags under vacuum

M. Guo *, S. Parada, P.T. Jones, J. Van Dyck, E. Boydens, D. Durinck, B. Blanpain, P. Wollants

Department of Metallurgy and Materials Engineering, Katholieke Universiteit Leuven, Kasteelpark Arenberg 44, BE-3001 Leuven, Belgium

Received 30 January 2006; received in revised form 14 February 2006; accepted 13 March 2006
Available online 27 June 2006

Abstract

The corrosion behaviour of a pitch-bonded magnesia-carbon refractory by an Al_2O_3 rich (~15 wt.%) stainless steelmaking slag was investigated by rotating finger tests in a vacuum induction furnace at high temperature (>1650 °C) and low oxygen partial pressure (1.5–4.3 × 10^{-10} atm). This study confirms the poor slagline behaviour of MgO-C bricks industrially observed in VOD ladles. Higher temperatures and longer exposure times lead to more severe slag infiltration and direct MgO dissolution. The intrinsic MgO-C reaction is the major decarburisation mechanism, while extrinsic decarburisation by oxygen from the atmosphere and/or reducible slag components (CrO_x, FeO_x) was limited. Three kinds of metallic particles with different size, shape, location, composition and origin were observed in the refractory specimens. Concurrently, the thermodynamic conditions for the formation of a protective $Mg(Al,Cr)_2O_4$ spinel layer at the slag/refractory interface are investigated. The industrial relevance of this spinel layer formation is discussed with respect to the chosen Al_2O_3 level. Guidelines are proposed to minimise MgO refractory dissolution in VOD slaglines.
© 2006 Elsevier Ltd and Techna Group S.r.l. All rights reserved.

Keywords: C. Wear resistance; C. Corrosion; D. MgO; E. Refractories

1. Introduction

Magnesia-carbon (MgO-C) refractories have been used successfully in basic oxygen (BOF) and electric arc furnaces (EAF). The reported advantage of MgO-C bricks lies in their high slag corrosion resistance attributable to (a) carbon's non-wettability which limits liquid slag penetration [1–3]; (b) formation of a dense MgO layer at the slag/brick interface, physically preventing slag ingress [4–6]; (c) reduction of iron oxide by C to Fe metal avoiding the attack of refractory oxides by iron oxide [7] and (d) generation of CO and/or Mg vapour providing an overpressure resisting slag/metal infiltration [8]. The combination of these mechanisms and their low cost have made MgO-C bricks one of the most successful refractory materials currently available for primary steel refining.

However, it is not straightforward to extrapolate the sound performance of MgO-C bricks in primary steelmaking environments (BOF, EAF) to secondary steelmaking applications. For instance, Baker et al. [9] pointed out that due to the low oxygen pressure in the argon oxygen decarburisation (AOD) or vacuum oxygen decarburisation (VOD) processes the conditions for the formation of a protective MgO layer are not met within the brick. Quon and Bell [10] conducted slag resistance tests on MgO-C bricks containing 15–24 wt.% carbon in vacuum at 1700 °C and found a substantial loss of MgO in the brick due to the interaction between magnesia grains and carbon. No MgO dense layer at the slag/brick interface was observed, suggesting that the gaseous Mg had been completely removed under vacuum.

Does this mean that MgO-C bricks cannot be used in VOD ladles? A limited number of industrials trials by the present

* Corresponding author. Tel. +32 16321279; fax: +32 16321991.
E-mail address: Muxing.Guo@mtm.kuleuven.be (M. Guo).

0272-8842/$32.00 © 2006 Elsevier Ltd and Techna Group S.r.l. All rights reserved.
doi:10.1016/j.ceramint.2006.03.009

Table 1
Experimental parameters and refractory materials for rotating finger tests in a vacuum induction furnace

Exp. no.	Time (min)	Temperature (°C)	P_{O_2} (atm)	Refractory materials	Others
Test 1	15	1710	4.28×10^{-10}	Pitch-bonded MgO-C	Steel amount: 15 kg; Slag amount: 1 kg
Test 2	35	1710	4.28×10^{-10}		Rotating speed: 12 rpm; pressure: 5 mbar
Test 3	45	1650	1.48×10^{-10}		Sample size: Ø32 mm × 150 mm

authors [11] did indeed show that MgO-C bricks performed poorly in VOD slaglines. Only in the low-wear locations in the VOD ladles (bottom and lower metal bath) could they replace the expensive and environmental-unfriendly direct-bonded magnesia-chromite refractories.

Notwithstanding the limited success of previous trials, this paper is a continued effort to expand the use of MgO-C bricks to VOD slaglines. Instead of performing additional industrial trials, laboratory tests are carried out. Although industrial trials will always remain indispensable, they are associated with a number of shortcomings. First of all, they are costly and hazardous, thereby limiting the amount of actual test runs. Secondly, a number of important parameters cannot be controlled in the industrial environment, and thirdly due to the multivariate character of the obtained data it is practically impossible to find out the role played by a specific parameter in industrial tests.

For instance, the previously mentioned industrial trials only investigated a VOD slag practice using CaO–SiO_2–MgO–Al_2O_3–Cr_2O_3 (CSMA–Cr_2O_3) slags containing low levels of Al_2O_3 (<8 wt.%). The investigation of the influence of Al_2O_3-rich slags on the performance of MgO-C bricks is, however, worthwhile for a number of reasons. On the one hand, such slags can be particularly interesting for metallurgical reasons. Enhanced Al_2O_3 levels increase the lime solubility and hence the sulphide capacity of the slag, thus improving the desulphurisation process during the production of stainless steel. Furthermore, an industrial observational study has suggested that higher Al_2O_3 levels may contribute to a better chromium recovery during the reduction stage in the stainless steel EAF process and thus probably also in VOD refining [12]. On the other hand, Al_2O_3-rich stainless steelmaking slags may offer a protective effect to slagline MgO-C refractories by changing the corrosion mechanism from direct dissolution to slower indirect dissolution of MgO into the slag.

In the present paper, rotating refractory finger tests are performed in a vacuum induction furnace where the VOD-reduction conditions can be closely simulated. The refractory wear and the oxidation behaviour of refractory carbon are discussed and compared with degradation mechanisms in industrial VOD linings and other investigations reported in the literature. The formation of distinct types of metal droplets encountered during the corrosion processes is highlighted. Specific attention is given to the conditions for the formation of a protective spinel layer at the slag/brick interface and its industrial relevance is discussed in association with the (in)direct dissolution of MgO.

Table 2
Chemical composition of the (as-delivered) VOD slag initially charged in the experiments as determined by ICP-AES (in wt.%)

MgO	Cr_2O_3	Al_2O_3	FeO	CaO	SiO_2	MnO	TiO_2
13.2	8.1	1.8	1.1	28	45	1.8	<0.5

2. Experimental

2.1. Experimental method

Rotating finger tests were performed in a vacuum induction furnace (type VSG 30, 60 kW power supply, 4 kHz frequency). Cylindrical refractory specimens (diameter = 32 mm; length = 150 mm) were dipped into the corrosive slag and liquid stainless steel, and rotated at 12 rpm. The experimental set-up and the procedure have been reported in previous work [13]. The experimental conditions are listed in Table 1. An alumina-chrome crucible (composition: 93 wt.% Al_2O_3, 3.9 wt.% Cr_2O_3; dimensions: Ø175 mm × 220 mm) was used to obtain the required high Al_2O_3 content slags. Approximately 15 kg of stainless steel (AISI 316), 1 kg of VOD-reduction slag (Table 2) supplied by a stainless steel company and a commercially available pitch-bonded MgO-C refractory (5.5 wt.% residual C) were used in the tests. The chemical composition and physical properties of the MgO-C specimens are given in Table 3. In order to simulate the atmosphere in the VOD process, a gas mixture of CO and CO_2 was blown into the furnace at flow rates of 30 l/min CO and 1 l/min CO_2. The oxygen partial pressure was thus set to be $\sim 10^{-10}$ atm. Three tests were carried out at distinct temperatures (Test 1 and 2: 1710 °C; Test 3: 1650 °C) with exposure times of 15, 35 and 45 min, respectively.

In order to remove any volatile species from the bricks, prior to the actual experiments the refractory fingers were placed in a graphite container with carbon and coked in the vacuum induction furnace at 1200 °C for 24 h. To clarify the temperature gradient in the melt and to obtain a better understanding of the temperature influence on slag/refractory

Table 3
Chemical composition and physical properties of pitch-bonded magnesia-carbon refractory finger specimens (as-delivered)

Chemical composition (mass%)	Physical properties
92MgO	Bulk density: 3.1 g/cm^3
5.5C	Apparent porosity: 6.0 vol.%
<1SiO_2	Cold crushing strength: 40 N/mm^2
<0.7Fe_2O_3	–

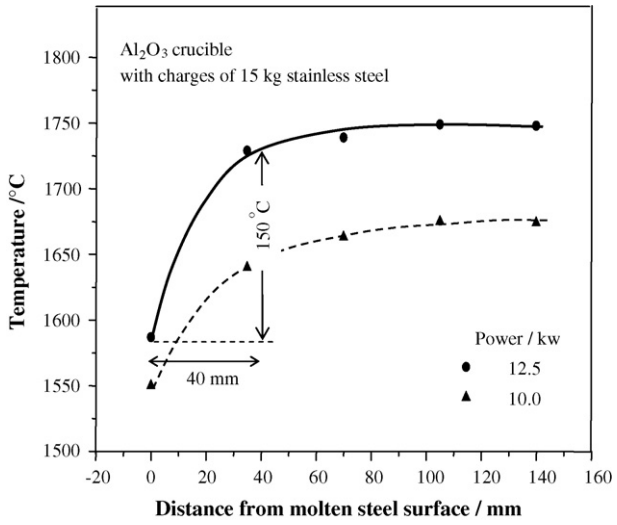

Fig. 1. Temperature profile of molten steel bath in the experiments.

interactions, a temperature profile of the crucible with a charge of 15 kg of stainless steel was measured in a separate melting test as shown in Fig. 1. A higher experimental temperature leads to a larger temperature gradient in the melt. In the present temperature range (1650–1710 °C), the bottom slag zone was around 150 °C hotter than the top slag zone as the thickness of the slag zone was around 40 mm (see solid line in Fig. 1). The top and bottom slag zone correspond, respectively, to the gas/slag and slag/metal interface.

2.2. Sample analysis techniques

The worn cylindrical refractory fingers were sliced into three pieces with a diamond saw. The slag zone sample was used for post-mortem assessment. To evaluate the corrosion behaviour in the different positions along the direction perpendicular to the slag surface, two specimens were prepared from all slag zone samples. These consisted of the cross section at the top (CHS) and the bottom (CHM) part of the slag zone. The details of the analysis techniques, including semi-quantitative SEM-EDS [14] and electron probe micro analysis (EPMA) EDS analyses [11] and slag analysis with inductively coupled plasma atomic emission spectroscopy (ICP-AES) [15], have been given in previous work. Slags attached to the refractory specimens surface and those infiltrated into bricks were measured with semi-quantitative SEM-EDS analyses (Table 4). The results were obtained from at least four global analyses of the slag areas (selected scans covering ~2500 μm^2 per analysis).

Table 4
Compositions of slag layer covered on the sample surface after completion of the test and composition of the infiltrated slag as determined by SEM-EDS (in wt.%)

Samples	MgO	Al_2O_3	SiO_2	CaO	Cr_2O_3	C/S
CHS-1	21.0	15.6	29	29	5.4	1.0
	–	–	–	–	–	–
CHM-1	–	–	–	–	–	–
	15.4	*12.7*	*33*	*37*	*1.4*	*1.1*
CHS-2	18.5	15.3	30	31	4.5	1.0
	21.6	*10.0*	*34*	*33*	*1.9*	*1.0*
CHM-2	12.2	14.8	35	35	3.7	1.0
	15.6	*17.8*	*33*	*34*	–	*1.0*
CHS-3	17.6	12.0	32	34	4.6	1.1
	21.9	*3.1*	*37*	*38*	–	*1.0*
CHM-3	16.4	13.1	33	35	3.2	1.1
	17.9	*14.1*	*36*	*32*	–	*0.9*

Data in italics represents compositions of the infiltrated slag; values for MnO and FeO_x were constantly lower than 1 mass% and therefore not given here.

3. Results and discussions

3.1. Overview of worn MgO-C refractory fingers

Figs. 2–4 show the general overviews of the worn microstructures of the hot face specimens. The degradation mechanisms are characterised by various combinations of slag infiltration, direct MgO dissolution into the penetrated slag, erosion of periclase grains at elevated temperature, MgO-C reaction and 'extrinsic' oxidation of refractory carbon by reducible slag components (e.g., FeO_x, CrO_x). The corrosion phenomena are now described.

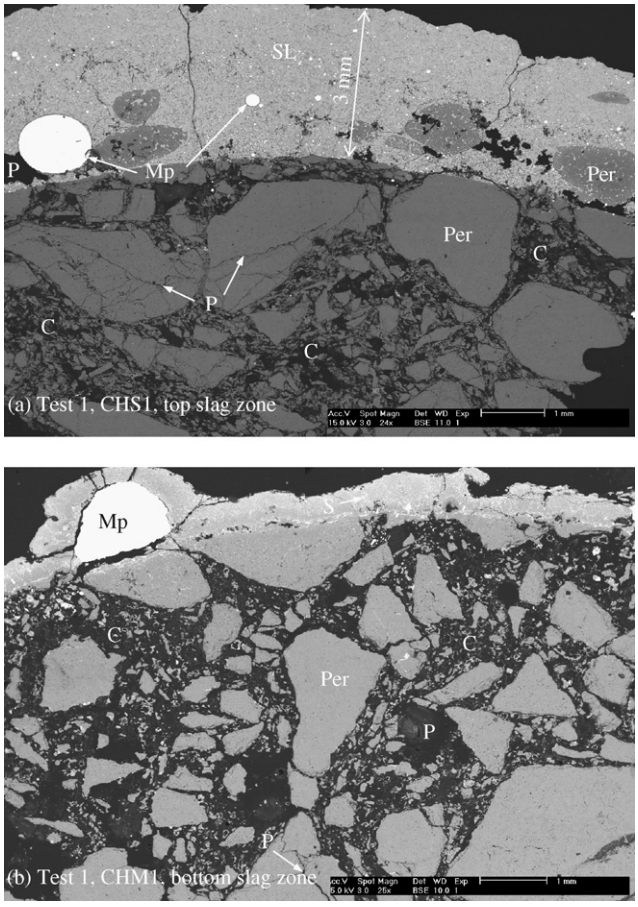

Fig. 2. Overview of worn samples of Test 1 showing the hot face of the top (a) and bottom (b) slag zone samples: (Per) magnesia (periclase); (C) carbon; (S) infiltrated slag; (SL) slag layer; (Mp) metallic particle; (P) pore or crack.

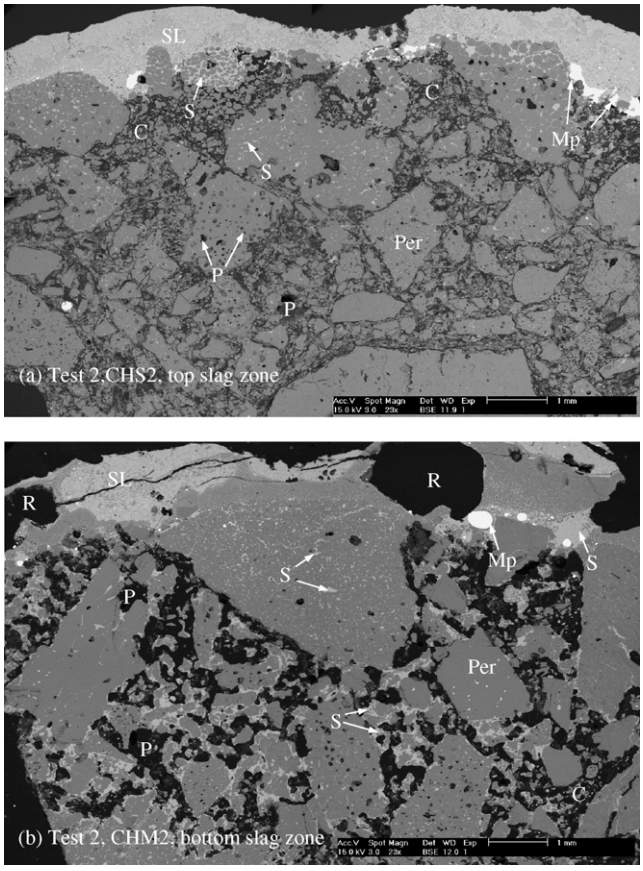

Fig. 3. Overview of worn samples of Test 2 showing the hot face of the top (a) and bottom (b) slag zone samples: (Per) magnesia (periclase); (C) carbon; (S) infiltrated slag; (SL) slag layer; (Mp) metallic particle; (P) pore or crack; MgO layer; (R) resin.

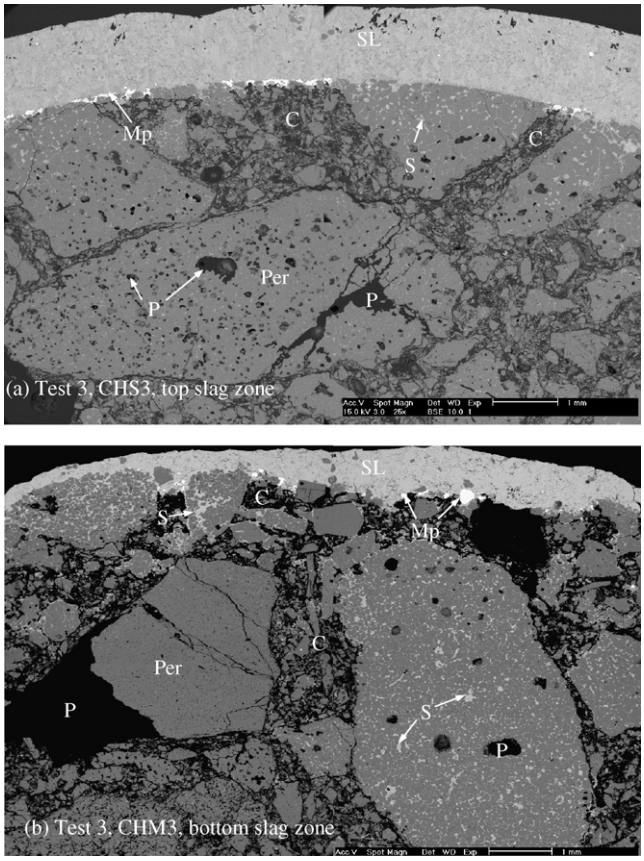

Fig. 4. Overview of worn samples of Test 3 showing the hot face of the top (a) and bottom (b) slag zone samples: (Per) magnesia (periclase); (C) carbon; (S) infiltrated slag; (SL) slag layer; (Mp) metallic particle; (P) pore or crack.

3.1.1. Test 1 (1710 °C, 15 min)

Fig. 2(a and b) are back scattered electron (BSE) images of the specimens for Test 1 at, respectively, the top (CHS1) and bottom (CHM1) slag zone. No slag infiltration is seen in the top slag zone sample. A slag layer of approximately 3 mm is observed on the brick surface, in which a number of detached periclase grains and a few large metallic particles can be seen. The former are thought to be periclase crystals previously removed from the bottom slag sample; the latter originate from the metal bath as their composition is almost identical as the charged stainless steel (in wt.%: 18Cr, 71.5Fe, 9.7Ni). The brick at the top slag zone remains almost intact owing to the short contact time with slag and the relatively low temperature in this zone.

No covering slag layer was observed on the surface of the bottom slag zone sample, presumably because of the higher slag fluidity at more elevated temperatures (1710 °C). The rough brick surface indicates a substantial erosion of the hot face periclase grains. This is due to the combined effect of high temperature softening of any intragranular silicate bond, and the strong stirring at the slag/metal interface caused by the metal induction.

3.1.2. Test 2 (1710 °C, 35 min)

Fig. 3a (top slag zone, CHS2) and b (bottom slag zone, CHM2) reveal a considerably modified microstructure of the corroded samples with longer interaction time. As compared to Test 1, decarburisation took place homogeneously over the entire specimen without an abrupt transition between a specific decarburised zone and the original carbon-containing region. As can be seen in Fig. 3, the loss of refractory carbon is significant, especially in the high temperature CHM2 sample. Simultaneously, a large number of pores and/or cracks were formed in the brick as a result of volumetric shrinkage associated with the decarburisation. In the top slag zone specimen (Fig. 3a), slag partially penetrated into the bricks along the intragranular grain boundaries of the (sintered) periclase crystals, while the carbon-containing zones remained intact. In the bottom slag zone (Fig. 3b), however, extensive slag infiltration occurred along the pores and cracks even at the center of the specimen. Similar to the bottom slag zone sample of Test 1 (Fig. 2b), the irregular surface of the hot face suggests that significant erosion occurs due to the elevated temperature imposed on it. As shown in Fig. 3a, the presence of a number of metallic particles close to the slag/refractory interface in contact with carbon, indicates that reducible slag compounds reacted with the refractory carbon.

3.1.3. Test 3 (1650 °C, 45 min)

These samples were less degraded than the samples of Test 2, as depicted in Fig. 4a (top slag zone, CHS3) and Fig. 4b (bottom slag zone, CHM3). The infiltration is limited to 2 mm

for the top slag zone sample. However, in the bottom slag zone specimen, infiltration is deeper. Slag layers were present both at the hot face of the top and bottom slag zone specimens. The different shapes of the slag/brick interface between the top and bottom slag zone specimens reveal the distinct degradation mechanisms for each sample position. An even slag/brick interface of the top slag zone sample (Fig. 4a) implies that little erosion occurred there, while in the bottom slag zone periclase grains were washed away from the brick surface and were scattered in the slag phase. The turbulence in the bottom slag zone gives rise to a washing effect that accelerates the hot erosion mechanisms. Similar to Test 2, large amounts of metal particles were found at the slag/brick interface because of the reaction between the refractory carbon and reducible slag components. In sample CHS3, a thin in situ formed spinel layer was also observed, which will be explained in detail later.

3.2. Slag penetration and refractory dissolution

3.2.1. Effects of corrosion time and temperature

Slag penetration can be quantified by Poiseuille's Law [16,17] which, although largely ignoring the influence of the refractory microstructure, does include the effect of slag viscosity which (indirectly) reflects the temperature effect. Lee and Zhang [7] highlight the importance of surface and interfacial energies on wetting leading to the following equation for slag infiltration:

$$L^2 = \left(\frac{r\cos\theta}{2}\right)\left(\frac{\sigma}{\eta}\right)t \quad (1)$$

where L is the slag penetration depth, r the open pore radius, η the slag viscosity, t the time, σ the slag surface tension and θ is the wetting or contact angle. According to Eq. (1), for a given slag/refractory system, the depth of slag penetration is a function of corrosion time and temperature (through slag viscosity). Slag penetration can take place only as temperature reaches a critical value, T_C, above which the slag is able to flow [18].

Due to the fact that a considerable temperature gradient existed along the slag zone during the tests, the temperature effect on the behaviour of slag infiltration can be understood through the comparison of worn microstructures in the different positions. Fig. 5 presents BSE images of the specimens of Test 3 for distinct sample positions. As can be seen from Fig. 5a (top slag zone), slag penetrated into the refractory finger confined in the hot face region while the centre part of the sample remained intact (Fig. 5b). At the bottom slag zone, however, slag infiltrated from the hot face (Fig. 5c) right to the sample centre (Fig. 5d) where a liquid slag network inside the periclase grains was observed. For a given test, the local temperature at the different sample positions was the only variable parameter, so the temperature gradient along the slag zone is responsible for the distinct slag infiltration behaviour. This infiltration occurs primarily along the intragranular periclase grain boundaries and/or open pores in the bricks. Increasing temperatures enhance slag infiltration due to the decrease in slag viscosity as indicated by Eq. (1).

The variation of slag infiltration in the refractory as a function of corrosion time is demonstrated in Fig. 6. Concurrently, a significant decrease in the remaining carbon level was observed. The periclase grains were heavily attacked by the infiltrating slag in the test with longer corrosion time

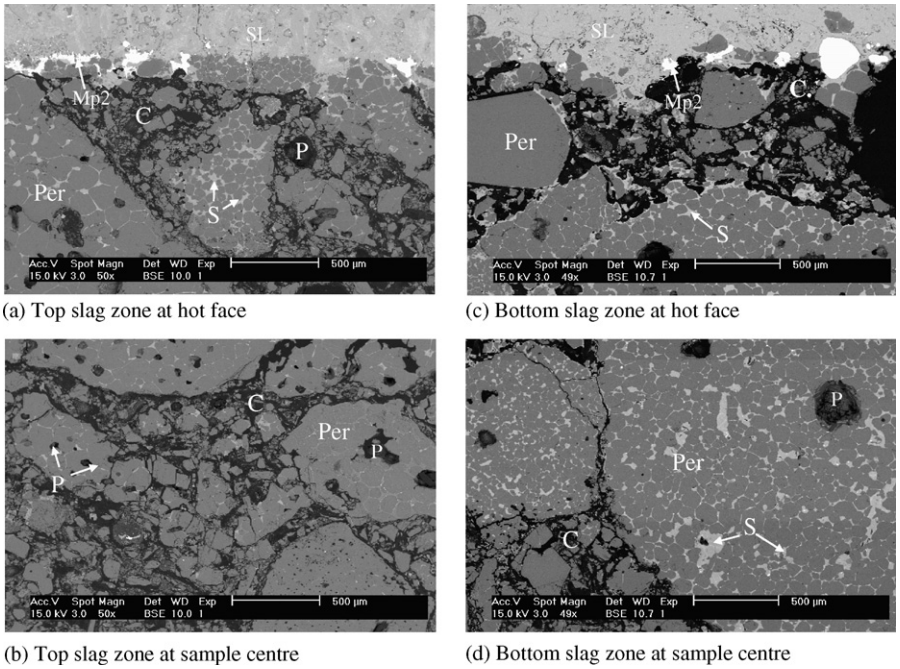

Fig. 5. BSE images of Test 3 at different positions, showing the temperature influence on the behaviour of slag infiltration: (Per) periclase; (C) carbon; (S) infiltrated slag; (SL) slag layer; (Mp2) type 2 metallic particle; (P) pore or crack. (a) Top slag zone at hot face; (b) top slag zone at sample center; (c) bottom slag zone at hot face; (d) bottom slag zone at sample center.

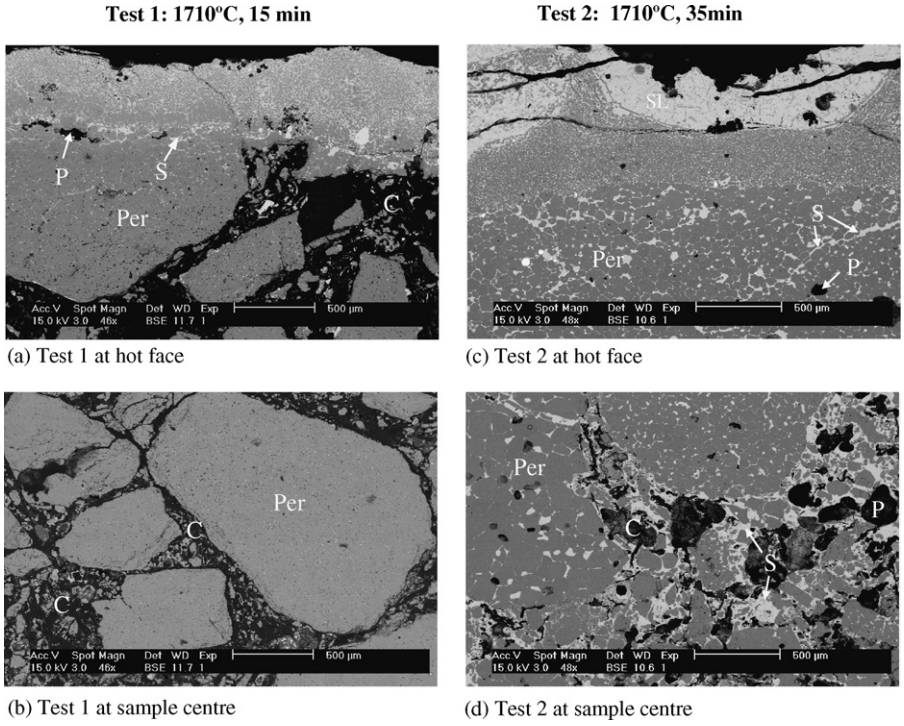

Fig. 6. BSE images of bottom slag zone samples of Test 1 (1710 °C, 15 min) and Test 2 (1710 °C, 35 min) at different positions, showing influence of interaction time on the behaviour of slag infiltration: (Per) periclase; (C) carbon; (S) infiltrated slag; (SL) slag layer; (P) pore or crack. (a) Test 1 at hot face; (b) Test 1 at sample center; (c) Test 2 at hot face; (d) Test 2 at sample center.

(Test 2: 1710 °C, 35 min) in which carbon failed to retard the slag penetration efficiently. Fig. 6d reveals that carbon in contact with the infiltrated slag was clearly observed in the sample center. This phenomenon was also found by Kim and Lu [6] and Baker et al. [9] in, respectively, laboratory tests and an AOD vessel lining. As can be seen in Fig. 6a and b, for the test with a shorter corrosion time (Test 1: 1710 °C, 15 min) only a shallow zone (Fig. 6a) was infiltrated by slag; other parts of the brick (Fig. 6b) remained intact. The time-dependency of slag infiltration relies on the kinetic conditions of the slag/refractory interaction system. Physical properties of MgO-C bricks, which are related to mass transport, such as bulk density and apparent porosity, strongly affect the slag infiltration rate. The loss of carbon in the brick results in a very porous region, which can easily be penetrated by the slag as seen in the bottom slag sample of Test 2 (Fig. 3b).

3.2.2. MgO dissolution into slag

Refractory dissolution in the slag phase inevitably occurs whenever the infiltrating slag is not saturated with certain components (e.g., MgO). This was substantiated in the present experiments by comparing the compositions of the slag layers attached to the sample hot faces with those of the infiltrated slag inside the refractory fingers. SEM-EDS analyses reveal that the MgO content of the infiltrated slag is on average 2 wt.% higher than that of the slag layers on top of the hot face as shown in Table 4 (data in italics are compositions of the infiltrated slag). Matsui et al. [19] found that the (direct) dissolution of MgO into the slag is a diffusion-controlled process.

3.3. Oxidation of refractory carbon

3.3.1. MgO-C reaction

Decarburisation of a carbon-containing brick is an important mechanism of refractory degradation. Depending on both the temperature and the atmosphere in the reaction system, decarburisation in MgO-C refractories can occur via carbon burnout by oxygen (direct oxidation):

$$2C(s) + O_2(g) = 2CO(g); \quad \Delta G_2^\circ = -114400 - 85.77T \quad (2)$$

and/or through the MgO-C reaction (indirect, intrinsic oxidation):

$$MgO(s) + C(s) = Mg(g) + CO(g); \quad \Delta G_3^\circ = 615600 - 289.77T \quad (3)$$

where the data for ΔG_2° and ΔG_3° (in J/mol) were taken from Engh [20]. The experimental observations verified that the MgO-C reaction occurred under the present test conditions. During the tests, a substantial volume of Mg vapour condensed as MgO in the cooler parts of the vacuum chamber, suggesting MgO loss occurs in the bricks due to the MgO-C reaction. In none of the tests, was an abrupt decarburised zone seen at the refractory hot face. This implies insufficient external oxygen from the gas phase and/or reducible slag components was supplied to the refractory hot face in order to form a decarburised layer at the refractory hot face. This indicates that the MgO-C reaction was predominant with reference to both the direct carbon burnout by oxygen gas and extrinsic carbon oxidation by reducible slag components. As the MgO-C reaction

proceeds, a number of pores or cracks are formed in the brick as a result of volumetric shrinkage. This facilitates both the slag infiltration and the removal of CO gas and Mg vapour generated during the reaction, accelerating refractory wear.

3.3.2. Extrinsic oxidation of refractory carbon and distinct metal particle types

Mathematical analyses by Kim and Lu [6] suggest that carbon in the brick is also oxidised by CO_2 (or indirectly by FeO), depending on temperature and the iron oxide activity in the slag. Based on experimental observations, Li et al. [21] concluded that CO/CO_2 gas bubbles are formed mainly by reaction between iron oxide in slag and carbon in the MgO-C refractory. Recently, the present authors [11] studied the behaviour of MgO-C refractories in VOD ladle linings and found that the oxidation of carbon took place in bricks where there was contact between infiltrating CrO_x-rich slag and refractory carbon, thereby forming metal particles rich in Cr (>60 wt.%) with lower amounts of Fe (5–40 wt.%) and Mn (<3 wt.%).

As summarised in Table 5, a number of metallic particles with distinct size, shape and composition were observed in the present experiments. 'Type 1 metal particles' are large (50–1000 μm), globularly shaped and have the same composition as stainless steel. They were detected in the specimens of Test 1 and 2. Most of Type 1 metal particles are present inside the slag covering the surface: they originate from droplets of liquid steel entrained into the slag during the test.

As can be seen in the general overview images (Figs. 3a, and 4a and b), a number of metal particles with irregular shape in contact with refractory carbon were observed in the samples of Test 2 and 3. These 'Type 2 metal particles' are mainly located at the slag/brick interface and are rich in chromium (~85 wt.%) and relatively poor in iron (~15 wt.% Fe). They are formed by the oxidation of refractory carbon by chromium and iron oxides in the slag, and are thus very similar as the particles observed in industrial applications [11]. FeO_x is only present in minor amounts in the slag of the present tests, resulting in metal particles that are rich in chromium but poor in iron. Fig. 7 presents the micrographs that reveal the reaction front between slag and carbon. These reactions can be expressed as:

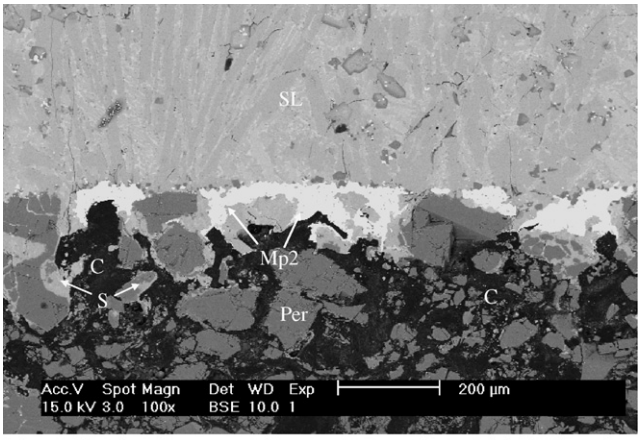

(a) Metallic phase in contact with amorphous carbon at brick/slag interface

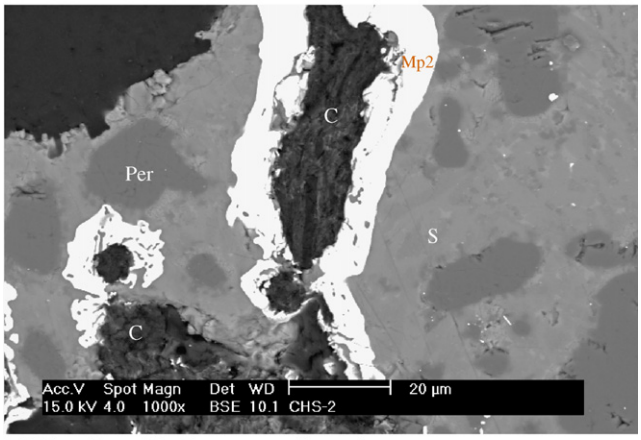

(a) Ring of metallic phase surrounding carbon

Fig. 7. Backscattered electron images of chromium-rich large metal phase (type 2 metallic particle) at carbon-slag reaction front: (Per) periclase; (C) amorphous carbon; (S) infiltrated slag; (Mp2) type 2 metallic phase. (a) Metallic phase in contact with amorphous carbon at brick/slag interface; (b) ring of metallic phase surrounding carbon.

$$(Cr_2O_3)_{slag} + 3C(s) = 2Cr(l) + 3CO(g) \quad (4)$$

Table 5
Composition of metallic particles resulting from reduction of slag components as determined by SEM-EDS (in wt.%)

Sample	Cr	Fe	Si	Mn	Ni	Particle characteristics
CHS-1	18.2	72	1.2	–	8.8	Size: 50–1000 μm; shape: globular; location: surface covering slag
CHM-1	18.6	72			9.1	
CHM-2	26.2	58	8.3	–	7.3	
CHS-2	85	14.8	–	–	–	Size: 10–500 μm; shape: amorphous; location: in contact with carbon at slag/refractory interface
CHS-3	89	10.8	0.2	–	–	
CHM-3	86	14.4				
CHS-1	57	43	0.5	–	–	Size: 0–10 μm; shape: globular; location: at periclase grain/infiltrated slag interface
CHM-1	38	60	1.1	1.1	–	
CHS-2	39	58	3.0	–	–	
CHS-3	52	48	0.7	–	–	
CHM-3	30	70	–	–	–	

$$(CrO)_{slag} + C(s) = Cr(l) + CO(g) \quad (5)$$

$$(FeO)_{slag} + C(s) = Fe(l) + CO(g) \quad (6)$$

For reactions (4)–(6) to proceed continuously, the reactants (chromium and iron oxides in the slag) must be transferred to the reaction sites (slag/carbon interface) while the reaction products (CO gas bubbles) need to be constantly formed and removed from the reaction front. As the non-wetting nature of carbon by the slag helps the CO gas bubbles to nucleate and grow, the above reactions will preferentially occur at the slag/carbon interface. This viewpoint was substantiated by Li et al. [21] who performed direct observations with a high temperature X-ray radiographic technique. The reduction of reducible slag components preferentially takes place along the carbon surface in the bricks (Fig. 7), causing precipitation of a metallic Cr–Fe phase in the vicinity of carbon, therefore resulting in irregular metal particles with relatively large size (around 10–500 μm). The low amount of Type 2 particles present inside the brick is due to the fact that the oxidation of carbon by CrO_x (and FeO, MnO) requires the presence of substantial amounts of liquid slag inside the brick. As estimated by the present authors [11], for a VOD slag, 1 vol. of carbon would approximately require 10–100 vol. of slag for its complete reaction. This explains why Type 2 metal particles are mainly located at the slag/brick interface where oxygen is continuously supplied through the influx of fresh liquid slag. However, since no explicit decarburisation layer was observed at the hot face, the oxidation of refractory carbon through the present mechanism is thought to be rather limited, in comparison with the MgO-C reaction.

Fig. 8 shows 'Type 3 metal particles' present at periclase grain boundaries in a slag 'matrix'. Most of them have a small particle size (0.5–10 μm) and are globularly shaped and attached to the periclase grains. Their dissimilar geometrical characteristics and different chemical composition (iron-rich Fe–Cr alloy, Table 5) with reference to Type 2 metal particles, in combination with the absence of carbon in their generation, imply a distinct formation mechanism: Mg and CO gas is first generated inside the brick through the MgO-C reaction. Slag infiltrates the bricks along the intragranular periclase grain boundaries where the infiltrating slag encounters the outward flowing magnesium vapour, resulting in the following reactions:

$$(Cr_2O_3)_{slag} + 3Mg(g) = 2Cr(l) + 3MgO(s) \quad (7)$$

$$(CrO)_{slag} + Mg(g) = Cr(l) + MgO(s) \quad (8)$$

$$(FeO)_{slag} + Mg(g) = Fe(l) + MgO(s) \quad (9)$$

Since Cr^{+3} in the slag will first be reduced to the divalent state under the present highly reducing and elevated temperature conditions, reactions (8) and (9) in particular will contribute to the chromium and iron metallisation. The reason why the particles are rich in iron and poor in chromium is due to the fact that at the initial stage iron oxide reduction occurs preferentially with respect to chromium oxide reduction (see Ellingham diagram [22]). Similarly, this preferential reduction of iron oxide was observed by Soykan et al. [23] in the reduction by graphite of a natural chromite ore.

The presence of small size particles attached to the periclase/slag interface (Fig. 8) indicates that the nucleation of liquid metal droplets took place heterogeneously at gas-filled (Mg and CO vapour) cavities or crevices on the periclase/slag interfaces, and that reactions (7)–(9) were just in an early stage. Type 3 particles are considerably smaller than the Type 2 metal particles due to a relative scarcity in reactants as compared to the available nuclei.

3.4. Formation of a spinel layer

High-temperature dissolution of MgO into CSMA-based slags can be direct or indirect, depending on whether or not a spinel layer forms at the periclase/slag interface. The occurrence of indirect dissolution could imply a lower wear rate of the MgO-C bricks in the VOD slagline, possibly enhancing their overall performance. However, only at the slag/brick interface in the top slag zone specimen of Test 3 (CHS3)

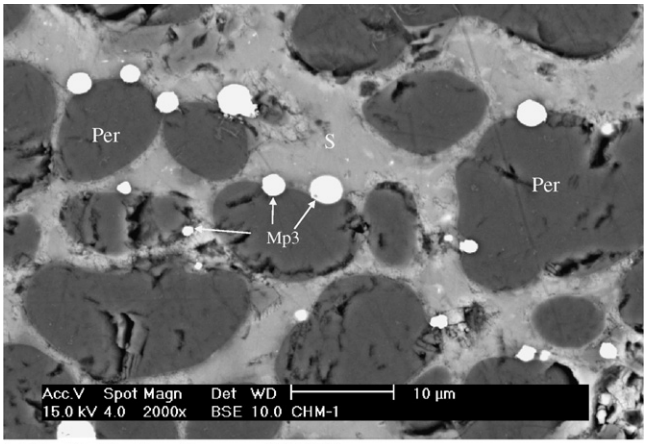

(a) Test 1 at bottom slag zone (CHM1)

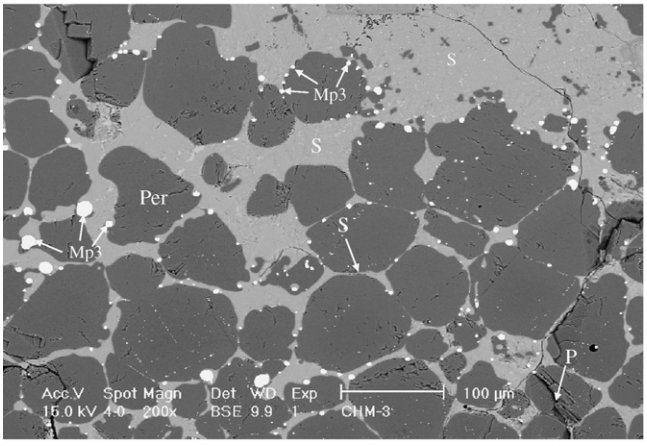

(b) Test 3 at bottom slag zone (CHM3)

Fig. 8. BSE images of iron-rich small globular metallic particles (type 3 metallic particle) between infiltrated slag and periclase grains: (Per) periclase; (C) carbon; (S) infiltrated slag; (Mp3) type 3 metallic particle. (a) Test 1 at bottom slag zone (CHM1); (b) Test 3 at bottom slag zone (CHM3).

was such a solid spinel layer (20–50 μm thick) found (Fig. 9a). As the final slag composition (Al_2O_3 and Cr_2O_3 content and C/S ratio) was almost identical for the different tests, this implies that temperature (apart from time) was the only variable parameter. Taking the vertical temperature gradient over the refractory fingers into account, the temperature of the CHS3 sample can be estimated to be in the vicinity of 1500 °C, while that of CHS1 and CHS2 was approximately 1560 °C. In the two latter samples, the spinel layer was not formed. The same is valid for the (warmer) bottom slag zone specimens (CHM1, 2 and 3). The reason for this different behaviour is now investigated.

3.4.1. Composition

The formation of a $Mg(Al,Cr)_2O_4$ spinel phase through contact between periclase and CSMA-Cr_2O_3 slag can be illustrated by the reactions:

$$MgO(s) + (Al_2O_3) = MgAl_2O_4(s) \quad (10)$$

$$MgO(s) + (Cr_2O_3) = MgCr_2O_4(s) \quad (11)$$

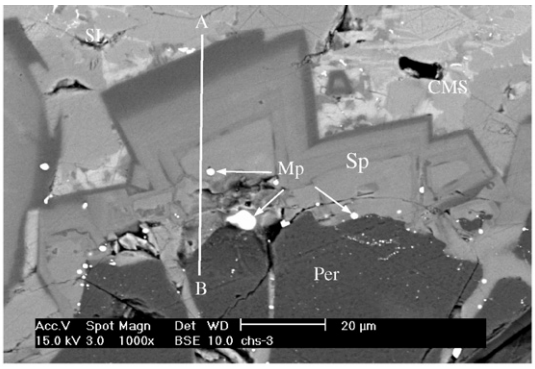

(a)BSE image of (Mg) (Cr, Al)$_2O_4$ spinel layer formed at slag /refractory interface: Per = periclase; Mp = precipitate of Cr-rich metal; SL = slag layer; Sp = spinel layer; CMS = CaO MgO SiO_2;1-3 = spinel phases with distinct compositions as shown in Table 6.

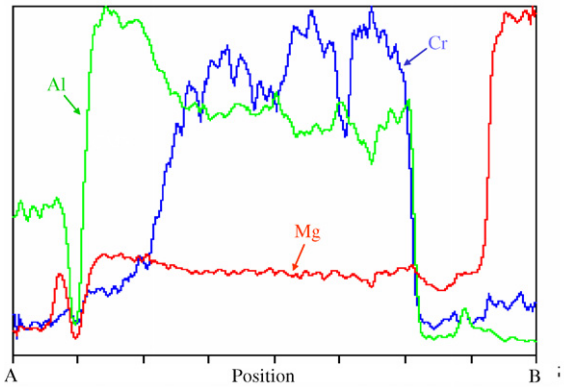

(b) Concentration profiles along the line A-B in (a) BSE image

Fig. 9. A spinel layer formed at slag /refractory for the sample of CHS3: (a) BSE images of (Mg) (Cr, Al)$_2O_4$ spinel layer, (b) concentration profiles along the line A–B in (a) BSE image. (a) Backscattered electron images of $Mg(Cr,Al)_2O_4$ spinel layer formed at slag/refractory interface: (Per) periclase; (S) infiltrated slag; (Mp) precipitate of Cr-rich metal; (SL) slag layer; (Sp) spinel layer; (CMS) CaO·MgO·SiO_2; (C_3MS_2) 3CaO·MgO·2SiO_2; (1–3) spinel phases with distinct compositions as shown in Table 4.

where the parentheses indicate a species dissolved in the slag. Semi-quantitative analyses of the spinel layer in CHS3 show that it is $Mg(Al,Cr)_2O_4$ spinel composed of approximately 46–69 wt.% Al_2O_3, 24–25 wt.% MgO and 5–30 wt.% Cr_2O_3. X-ray line analyses (Fig. 9b) reveal that the MgO content across the spinel layer remains unaltered while the Cr_2O_3 content increases substantially with a simultaneous decrease in the Al_2O_3 level closer to the magnesia refractory surface (along the path A–B). The metal particles in Fig. 9a, on the other hand, are the result of the decomposition of Cr_2O_3 both in the hot face periclase solid solution and in the spinel. This is a phenomenon that is caused by the low oxygen pressure ($\sim 10^{-10}$ atm), which has also been observed in post-mortem studies of magnesia-chromite refractories in VOD ladles [24].

3.4.2. Phase diagram analysis

The critical conditions for generating this spinel layer can be understood using the phase diagram analyses proposed by Zhang and Lee [25]. They assessed the possibility of $MgAl_2O_4$ spinel formation at high temperature in CSMA slags using the quaternary CSMA phase diagrams with 5, 10, 15, 20, 25, 30 and 35 wt.% Al_2O_3 (see Fig. 10 for 15 and 25 wt.% Al_2O_3). As no $MgAl_2O_4$ spinel liquidus surface appears in the CSMA

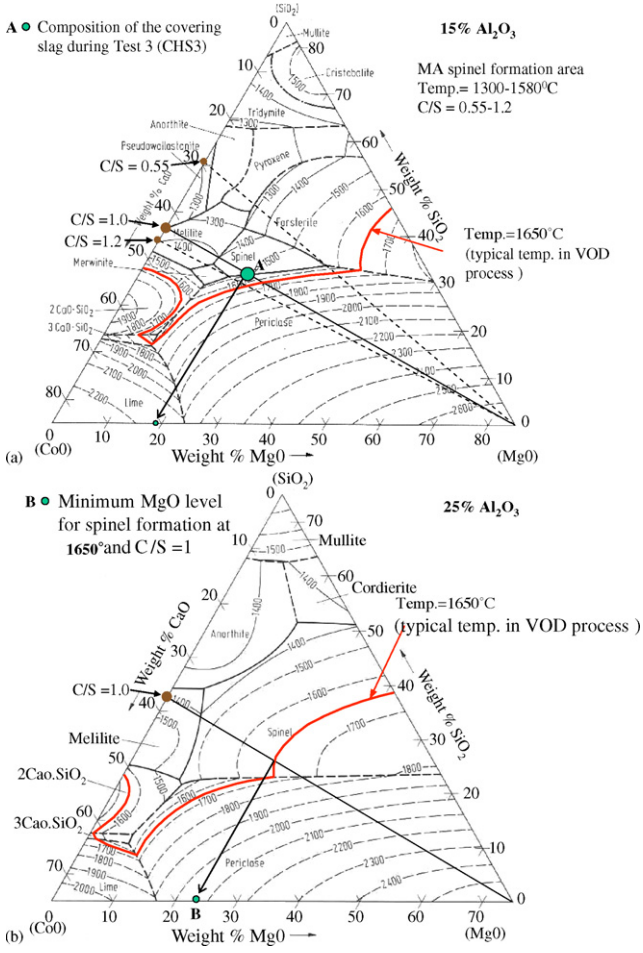

Fig. 10. (a and b) Phase relations at liquidus temperature in (a) 15 wt.% and (b) 25 wt.% Al_2O_3 content planes of CaO–MgO–Al_2O_3–SiO_2 system, showing the areas for MgO·Al_2O_3 (MA) spinel formation. (a) 15% Al_2O_3; (b) 25% Al_2O_3.

diagrams with 5 or 10 wt.%, Zhang and Lee [25] concluded that the Al_2O_3 content should at least be in excess of 10 wt.%. Apart from higher Al_2O_3 levels, lower basicities favour spinel formation.

A similar approach is followed here to qualitatively explain why in the colder sample CSH3 ($T \sim 1500$ °C) of Test 3 a spinel layer was found but not in the hotter bottom slag zone specimen CHM3 ($T \sim 1650$ °C). As in the present system the obtained spinel phase also contains Cr_2O_3, an assumption needs to be made in order to make use of the CSMA phase diagram analysis. Considering that Cr^{3+} takes up the same octahedral position as Al^{3+} in the $Mg(Al,Cr)_2O_4$ spinel structure and is mutually exchangeable [24], it is a reasonable assumption to work with the combined level of Cr_2O_3 and Al_2O_3 in the slag and express this as the 'Al_2O_3' content to be used in the phase diagram analysis. Using the (covering) final slag compositions of Table 4, this 'Al_2O_3' level for CHS3 (CHM3) adds up to 16.6 (16.3) wt.%, so that the CSM–15% Al_2O_3 is the closest match available. The slag basicity (C/S ratio) approximates unity. With the CSM–15% Al_2O_3 phase diagram (Fig. 10a) it can be estimated that for Test 3 the spinel liquidus surface extends from 1400 to 1500 °C. For spinel to form in situ the MgO content needs to be around 17–18 wt.%. At lower values the slag composition is situated above the MA liquidus surface and would thus be completely liquid at 1500 °C. The latter is also estimated to be the actual temperature to which CHS3 was exposed, thus tentatively explaining why spinel was found here. Fig. 10a corroborates that the covering slag has a composition of approximately 18 wt.% MgO (1500 °C, point A). The fact that in the higher temperature specimen (CHM3, 1650 °C), no spinel was found can also be explained by this figure. The slag with composition A would be completely liquid at 1650 °C. Using a similar approach it can be shown that, thermodynamically, no spinel can be formed at the conditions relevant for CHS1/2 (1560 °C, C/S ∼ 1, 'Al_2O_3' ∼ 20 wt.%) and CHM1/2 (1710 °C, C/S ∼ 1, 'Al_2O_3' ∼ 20 wt.%).

3.4.3. Industrial relevance

The potential formation of a protective spinel layer under VOD conditions is not only relevant for the performance of MgO-C bricks but for all magnesia-based systems (e.g., magnesia-chromite, magnesia-doloma). The experimental observations and the CSMA phase diagram analysis have suggested that for a slag basicity of unity and 15 wt.% Al_2O_3 the spinel formation temperature is approximately 1500 °C, i.e., 150 °C lower than typical VOD process temperatures. Nevertheless, higher Al_2O_3 levels in the slag (with the same C/S ratio) will increase the maximum formation temperature of spinel (larger $MgAl_2O_4$ spinel liquidus surface for higher Al_2O_3 levels, e.g., 25 wt.% in Fig. 10b). The required Al_2O_3 levels to form 'MA' spinel at VOD temperatures (e.g., 1650 °C) can be estimated with the CSMA (0–35 wt.% Al_2O_3) phase diagrams. Table 6 (see also Fig. 10a and b) shows the temperature range for the spinel liquidus surface (for C/S = 1) and the accompanying minimum MgO slag content to be situated under the spinel liquidus. For the Al_2O_3 contents where no spinel is formed, the MgO solubility is listed for a temperature of 1650 °C and a slag C/S ratio of unity. From this table, it can be seen that to obtain a passivating MgO layer at VOD conditions, the Al_2O_3 content needs to be in excess of 25 wt.%. However, in that case the minimum MgO level for spinel formation is around 23 wt.%. At 30 wt.% Al_2O_3 this value increases slightly to 24 wt.%. Even though one would obtain a passivating spinel layer, there would still remain a large thermodynamic driving force for continued indirect MgO dissolution. Note that in a VOD environment, the turbulence in the slag would result in rapid mass transport so that local slag compositions near the lining would resemble the bulk slag composition. As such a slag practice would require astronomical dolomite additions to protect the magnesia-based refractories in the VOD lining, this is obviously not advisable. Table 6 also shows that, at even higher Al_2O_3 levels (35 wt.%), the situation changes abruptly: in this case the required MgO level suddenly drops to 12 wt.%, which is in agreement with Zhang and Lee [25]. From a point of view of refractory protection, this would be interesting. However, the required Al_2O_3 level is unrealistically high as this could have other (unexpected) metallurgical side effects. From Table 6 one may conclude that it is preferable to work with slags with relatively low Al_2O_3 levels (e.g., 5–10 wt.%) for which MgO saturation solubilities are limited. This can be further optimised by targeting dual saturation (C_2S and MgO) at which MgO solubilities drop to values as low as 14 wt.% (C/S > 1, 1650 °C), as discussed in previous work [26]. Direct MgO dissolution can then be easily controlled by balanced MgO additions.

Table 6
MgO dissolution mechanism at 1650 °C for a VOD slag system with C/S = 1 and varying Al_2O_3 levels

Al_2O_3 level	T range spinel liquidus surface (°C)	Minimum MgO level for spinel formation at 1650°	MgO solubility (wt.%) at 1650 °C (at dual* saturation)	MgO dissolution mechanism at 1650 °C
0	–	–	23.5 (17)	Direct
5	–	–	24.5 (16)	Direct
10	–	–	23 (14)	Direct
15	1400–1500	–	23	Direct
20	1400–1620	–	26	Direct
25	1420–1680	23	–	Indirect
30	1400–1685	24	–	Indirect
35	1410–1830	12	–	Indirect

* Dual saturation refers to C_2S and MgO saturation, rendering minimum MgO solubility levels.

4. Conclusions

In order to assess the slagline wear of MgO-C bricks in contact with Al_2O_3 rich VOD-reduction slags, rotating finger tests were performed in a vacuum induction furnace. Cylindrical pitch-bonded MgO-C refractory samples were brought into contact with CSMA–Cr_2O_3 slags containing 12–17 wt.% Al_2O_3. The microstructure of the worn samples and their degradation mechanisms were investigated through post-mortem microstructural characterisation. The following conclusions can be drawn:

(1) Higher temperatures and longer exposure time lead to more severe slag infiltration and direct MgO dissolution. The (intrinsic) MgO-C reaction is the major decarburisation mechanism, while (extrinsic) decarburisation by oxygen from the atmosphere and/or reducible slag components (CrO_x, FeO_x) was limited. The MgO-C reaction is the main reason for the poor behaviour of this material under simulated VOD conditions.
(2) Three kinds of metallic particles with different size, shape, location, composition and origin were observed in the refractory specimens. Their distinct origin was discussed.
(3) The conditions for the formation of a passivating spinel layer were studied. Only at the slag/brick interface in the top slag zone specimen of Test 3 (CHS3), a zoned spinel layer was observed. Using quaternary CaO–MgO–SiO_2–Al_2O_3 phase diagrams, the spinel formation temperature was roughly estimated to be around 1500 °C, which is in agreement with the experimental observations. For a protective spinel layer to form in VOD conditions and to obtain (slow) indirect MgO dissolution, the Al_2O_3 level would have to be higher than 25 wt.%. Furthermore, this would require excessive MgO levels (>20 wt.%). Increasing the Al_2O_3 level to 35 wt.% abruptly decreases this MgO level to a value of 12 wt.% but such a Al_2O_3 concentration becomes unrealistically high. It is, therefore, advisable to work with dual (C_2S/MgO) saturated slags with an Al_2O_3 level of 5–10 wt.%, for which MgO solubilities lie in the range of 16–14 wt.% at 1650 °C.
(4) Finally, many mechanisms seen in industrial reality are also observed in the present laboratory experiments. The advantage of the lab set-up, however, lies in the possibility to target the investigation of the influence of specific parameters. The present experimental procedure is, therefore, an excellent tool for the study of refractory degradation mechanisms in industrial processes, allowing to diminish the risks associated with industrial plant trials.

Acknowledgements

This work was performed with the financial and technical support of U&A Belgium and the IWT (project no. 990348). The authors are grateful to the engineers of U&A Belgium for their close co-operation with our team. Practical advice from Heraeus Electro-Nite was much appreciated. Sander Arnout and Frederik Verhaeghe are acknowledged for their comments on spinel formation.

References

[1] H. Barthel, Effect of carbon in tar-impregnated burnt magnesite bricks on the wear of basic oxygen furnace linings, Stahl u. Eisen 86 (1966) 81–88.
[2] R.W. Limes, Refractories for basic oxygen furnace, J. Met. (1966) 865–869.
[3] R.H. Herron, C.R. Beechan, R.C. Padfield, Slag attack on carbon-bearing basic refractories, Amer. Ceram. Soc. Bull. 46 (1967) 1163–1168.
[4] G.D. Pickering, J.D. Batchelor, Carbon-MgO reactions in BOF refractories, Amer. Ceram. Soc. Bull. 50 (1971) 611–614.
[5] R.J. Leonard, R.H. Herron, Significance of oxidation-reduction reactions within BOF refractories, J. Am. Ceram. Soc. 55 (1972) 1–6.
[6] S.M. Kim, W.K. Lu, Kinetics mechanism of the formation of dense MgO layer in pitch-bearing magnesite brick during service, Met. Trans. 9B (1978) 353–364.
[7] W.E. Lee, S. Zhang, Melt corrosion of oxide and oxide-carbon refractories, Int. Mater. Rev. 44 (1999) 77–104.
[8] P.C. Robinson, Some observation on unused and used refractories from oxygen steelmaking vessels, J. Refractories 42 (1966) 218–222.
[9] B.H. Baker, B. Brezny, R.L. Shultz, The role of carbon in MgO refractories, Am. Ceram. Soc. Bull. 54 (1975) 665–666.
[10] D.H. Quon, K.E. Bell, Performance of magnesia-carbon bricks in vacuum at high temperature, J. Canad. Ceram. Soc. 56 (1987) 39–44.
[11] S. Smets, S. Parada, J. Weytjens, G. Heylen, P.T. Jones, M. Guo, B. Blanpain, P. Wollants, Behaviour of magnesia-carbon refractories in vacuum-oxygen decarburization ladle linings, Ironmaking Steelmaking 30 (2003) 293–300.
[12] M. Guo, D. Durinck, P.T. Jones, G. Heylen, R. Hendrickx, R. Baeten, B. Blanpain, P. Wollants, EAF stainless steel refining. Part I: Observational study on chromium recovery in an eccentric bottom tapping furnace and a spout tapping furnace, Steel Res. Int., submitted for publication.
[13] M. Guo, S. Parada, S. Smets, P.T. Jones, J. Van Dyck, B. Blanpain, P. Wollants, Laboratory study of the interaction mechanisms between magnesia-chromite refractories and Al_2O_3-rich VOD slags, in: Proceedings of the Seventh International Conference on Molten Slags, Fluxes and Salts, SAIMM, Cape Town, South Africa, (2004), pp. 327–336.
[14] M. Guo, S. Parada, S. Smets, P.T. Jones, E. Boydens, J. Van Dyck, B. Blanpain, P. Wollants, A Vacuum Induction Furnace Study of the Corrosion Mechanisms of MgO-C Refractories by Al_2O_3-Rich VOD Slags, in: Proceedings of the 43th Annual Conference of Metallurgists of CIM, Hamilton, Canada, (2004), pp. 687–701.
[15] P.T. Jones, P. Hermans, B. Blanpain, P. Wollants, Optimization of an accurate and precise analysis procedure for metallurgical VOD slags with ICP-OES, Atom. Spectrosc. 21 (2000) 86–92.
[16] Z. Yu, K. Mukai, K. Kawasaki, I. Furusato, Relation between corrosion rate of magnesia refractories by molten slag and penetration rate of slag into refractories, J. Ceram. Soc. Jpn. 101 (1993) 533–539.
[17] Y. Kuromitsu, H. Yoshita, H. Takebe, K. Morinaga, Interaction between alumina and binary glasses, J. Am. Ceram. Soc. 80 (1997) 1583–1587.
[18] S. Jansson, V. Brabie, L. Bohlin, Corrosion mechanism and kinetic behaviour of refractory materials in contact with CaO-Al_2O_3-MgO-SiO_2 slags, in: Proceedings of the Seventh International Conference on Molten Slags, Fluxes and Salts, Cape Town, (2004), pp. 341–347.
[19] K. Matusi, F. Kawano, K. Nibu, Reaction between magnesia and molten slag (Part I), Taikabutsu (Refractories) 43 (1991) 442–450.
[20] T.A. Engh, Principles of Metal Refining, Oxford University Press, Oxford, 1992.
[21] Z. Li, K. Mukai, Z. Tao, Reactions between MgO-C refractory. Molten slag and metal, ISI J. Int. 40 (2000) S101–S105.
[22] C.H.P. Lupis, Chemical Thermodynamics of Materials, North-Holland, 1983, p. 133.

[23] O. Soykan, R.H. Eric, R.P. King, The reduction mechanism of a natural chromite at 1416 °C, Met. Trans. 22B (1991) 53–63.
[24] P.T. Jones, Degradation Mechanisms of Basic Refractory materials during the Secondary Refining of Stainless Steel in VOD Ladles, PhD Thesis, Leuven, 2000.
[25] S. Zhang, W.E. Lee, Use of phase diagrams in studies of refractory corrosion, Int. Mater. Rev. 45 (2) (2000) 41–58.
[26] P.T. Jones, B. Blanpain, P. Wollants, B. Hallemans, G. Heylen, J. Weytjens, Extending the lining life of ALZ nv's ladle lining, Ironmaker Steelmaker 26 (12) (1999) 31–35.